

# Point defect distribution in high-mobility conductive SrTiO<sub>3</sub> crystals

---

Gentils, A.; Copie, O.; Herranz, G.; Fortuna, F.; Bibes, M.; Bouzehouane, K.; Jacquet, E.; Carretero, C.; Basletić, Mario; Tafra, Emil; ...

Source / Izvornik: **Physical review B: Condensed matter and materials physics**, 2010, 81

Journal article, Published version

Rad u časopisu, Objavljena verzija rada (izdavačev PDF)

<https://doi.org/10.1103/PhysRevB.81.144109>

Permanent link / Trajna poveznica: <https://urn.nsk.hr/urn:nbn:hr:217:711002>

Rights / Prava: [In copyright](#) / [Zaštićeno autorskim pravom.](#)

Download date / Datum preuzimanja: **2025-03-24**



Repository / Repozitorij:

[Repository of the Faculty of Science - University of Zagreb](#)



# Point defect distribution in high-mobility conductive SrTiO<sub>3</sub> crystals

A. Gentils,<sup>1,2</sup> O. Copie,<sup>3</sup> G. Herranz,<sup>3,4,\*</sup> F. Fortuna,<sup>1</sup> M. Bibes,<sup>3</sup> K. Bouzehouane,<sup>3</sup> É. Jacquet,<sup>3</sup> C. Carrétéro,<sup>3</sup> M. Basletić,<sup>5</sup> E. Tafrā,<sup>5</sup> A. Hamzić,<sup>5</sup> and A. Barthélémy<sup>3</sup>

<sup>1</sup>Centre de Spectrométrie Nucléaire et de Spectrométrie de Masse, CNRS-IN2P3-Université Paris-Sud 11, 91405 Orsay Campus, France

<sup>2</sup>CEMHTI Site Cyclotron, CNRS, 3A rue de la Férollerie, 45071 Orléans Cedex 2, France

<sup>3</sup>Unité Mixte de Physique CNRS/Thales associée à l'Université Paris-Sud, Campus de Polytechnique, 1 Avenue A. Fresnel, 91767 Palaiseau, France

<sup>4</sup>Institut de Ciència de Materials de Barcelona, ICMAB-CSIC, Campus de la UAB, Bellaterra 08193, Catalonia, Spain

<sup>5</sup>Department of Physics, Faculty of Science, University of Zagreb, Bijenička 32, P.O. Box 331, HR-10002 Zagreb, Croatia

(Received 20 January 2010; revised manuscript received 8 March 2010; published 13 April 2010)

We have carried out positron-annihilation spectroscopy to characterize the spatial distribution and the nature of vacancy defects in insulating as-received as well as in reduced SrTiO<sub>3</sub> substrates exhibiting high-mobility conduction. The substrates were reduced either by ion etching the substrate surfaces or by doping with vacancies during thin-film deposition at low pressure and high temperature. We show that Ti vacancies are native defects homogeneously distributed in as-received substrates. In contrast, the dominant vacancy defects are the same both in ion etched crystals and substrates reduced during the film growth, and they consist of nonhomogeneous distributions of cation-oxygen vacancy complexes. Their spatial extension is tuned from a few microns in ion-etched samples to the whole substrate in specimens reduced during film deposition. Our results shed light on the transport mechanisms of conductive SrTiO<sub>3</sub> crystals and on strategies for defect-engineered oxide quantum wells, wires, and dots.

DOI: [10.1103/PhysRevB.81.144109](https://doi.org/10.1103/PhysRevB.81.144109)

PACS number(s): 78.70.Bj, 61.72.J—, 61.80.Jh

## I. INTRODUCTION

Among perovskites, SrTiO<sub>3</sub> (STO) is one of the most widely studied oxides because of its potential in many applications in oxide electronics, including strain-induced ferroelectricity<sup>1</sup> and the insulator-to-metal transition induced by chemical doping.<sup>2</sup> Like any other oxide, this material is prone to host many types of defects among which oxygen vacancies have a preponderant role. These vacancy defects are well known to affect profoundly the physical properties via local changes in chemical composition and/or electronic configuration. Conspicuous examples are tunable filters for microwave devices, where point defects in STO have a strong influence on dielectric losses<sup>3</sup> or resistive switching, where vacancies are believed to drive the observed reversible electric pulse-induced changes in resistance.<sup>4,5</sup> There is an increasing interest, therefore, to study the defect chemistry in oxides, where vacancy-defect thermodynamics, oxygen transport, or vacancy-defect nature analysis are relevant issues.

Here we would like to emphasize a peculiar feature observed in vacancy-defect formation in STO and its relationship with electronic transport. In STO, oxygen vacancies modify drastically the electrical properties by changing the insulating character of stoichiometric STO into a good *n*-type conductor at concentrations as small as  $>10^{15}$  cm<sup>-3</sup>. These vacancy defects are believed to be ionized—oxygen vacancies are charged positively—releasing electrons into the conduction band, i.e., acting like donors. It is found that for certain carrier and defect concentrations, these carriers have electron mobility values above 10<sup>4</sup> cm<sup>2</sup>/V s at low temperatures,<sup>6</sup> among the highest in any oxide. While this behavior has been known since 1960s, a critical issue is now to tailor the spatial extension of this high-mobility electron

gas. Indeed, confinement over regions typically smaller than the Fermi wavelength of carriers would allow to form oxide-based low-dimensional structures such as quantum wires or quantum dots.

A way to introduce oxygen vacancies in STO single-crystal substrates consists in growing films on top of them at high temperature and low-oxygen partial pressure. This technique is sometimes referred to as “autofeeding epitaxy”.<sup>7</sup> These studies have proved that vacancies spread over large distances (the whole substrate) due to the fast diffusion of oxygen vacancies in STO in these growth conditions.<sup>7–10</sup> While the vacancy concentration can be controlled by the growth time,<sup>10</sup> their spatial distribution is hard to engineer. In this line, low-temperature generation of oxygen vacancies by means of Ar<sup>+</sup> ion etching of STO surfaces<sup>11,12</sup> has been demonstrated to yield conductive layers at the surface.

The purpose of our work has been to characterize the spatial distribution and nature of vacancy defects within the conductive layers of STO crystals displaying high-mobility conduction, either prepared by ion etching the surfaces or by doping with vacancies during thin-film deposition at low pressure and high temperature. At the same time, we have also analyzed the native defects in insulating as-received STO substrates. Because tiny amounts of oxygen vacancies can trigger substantial modifications of the physical properties of STO, positron-annihilation spectroscopy (PAS) techniques appear as an appropriate characterization tool, with sensitivity to concentrations as small as 0.01–1 ppm.<sup>13,14</sup> The detection of oxygen-vacancy complex defects by PAS techniques has been demonstrated in STO in previous reports.<sup>7,15–17</sup> For the purposes outlined in this work, we employed two different positron-annihilation spectroscopies: conventional positron lifetime and Doppler annihilation broadening coupled to a slow positron beam.

## II. EXPERIMENTAL: SAMPLE PREPARATION AND POSITRON-ANNIHILATION SPECTROSCOPY

In this section, we first describe the sample preparation and subsequently we give the details of PAS experiments. Regarding sample preparation, prior to any ion etching or film deposition, each as-received substrate (Crystec GmbH) was cut into two parts, and one of them was kept untreated and used as a reference for comparative purposes as well to analyze the nature of native vacancy defects. Two ion-etched samples were irradiated at room temperature with  $\text{Ar}^+$  ions accelerated at 300 eV during 1000 s (sample IE1000) and 10 s (IE10), respectively, with a current density of 0.5 mA/cm<sup>2</sup>. Freshly irradiated samples were conductive, with values of electronic mobility at low temperature  $\mu_{4\text{K}} \approx 6300 \text{ cm}^2/\text{V s}$  (IE1000) and  $\mu_{4\text{K}} \approx 3500 \text{ cm}^2/\text{V s}$  (IE10), similar to those reported in the previous literature.<sup>11,12</sup> However, quite strikingly, the sample IE10 showed a fast evolution with time, and in the scale of several days it became insulating, indicating a rapid reoxygenation of the oxygen-deficient surface. As described below, the vacancy-defect distribution in the IE10 sample also exhibits a fast evolution with time, consistent with transport. In addition to these ion-etched samples, we have also prepared samples consisting of Co-doped (La,Sr)/TiO<sub>3</sub> (LSTO) thin films deposited on STO single-crystal substrates by pulsed laser deposition at low pressure ( $P_{\text{O}_2} = 10^{-6}$  mbar) and high temperature ( $T = 750^\circ$ ). The samples analyzed here consisted of thin films with different thicknesses  $t = 10, 50$ , and 150 nm, designated as LSTO-10, LSTO-50, and LSTO-150, respectively. The transport properties of these samples are dominated by the properties of the STO substrate, which get doped with oxygen vacancies throughout all the volume and indeed display high-mobility conduction (typically well above  $10^3 \text{ cm}^2/\text{V s}$ ).<sup>9,10</sup> The reduction in the STO substrates scales with the film deposition time and thus, with film thickness.<sup>10</sup> Finally, we have also analyzed an *in situ* annealed LaAlO<sub>3</sub>(LAO)/STO sample (IA-LAO). This sample was grown at the same conditions for which a high-mobility conduction was found to be confined within a few unit cells next to the LAO/STO interface (see details in Ref. 18) in agreement with other reported works.<sup>19,20</sup> The interest of studying this LAO/STO sample is that, as shown below, the presence of oxygen-vacancy-related defects is strongly suppressed with respect to the as-received or treated STO substrates, making them suitable as a reference of the ideal vacancy-defect-free lattice.

PAS experiments were done at room temperature. Two PAS techniques were employed to characterize vacancy defects, using radioactive <sup>22</sup>Na isotopes as a positron source. First, we discuss briefly the positron lifetime measurements, which are based on the detection of  $\gamma$  photons with two different ranges of energy. On one hand, photons with energy 1.27 MeV emitted simultaneously with the positrons during the  $\beta^+$  decay of the <sup>22</sup>Na radioactive isotope are sensed; on the other hand, 0.511 MeV  $\gamma$  photons emitted during the positron-electron pair annihilation in the solid are also detected. Both measurements enable positron lifetime measurement by a start-stop coincidence  $\gamma$  spectrometer. The positron lifetime is a function of the electron density at the

annihilation site: when positrons are trapped in open-volume defects such as vacancies and their agglomerates, the positron lifetime increases with respect to that of the defect-free sample due to the locally reduced electron density. Measuring positrons lifetime spectra allows the identification of the nature of the vacancy-type defects in a solid.<sup>14</sup> In our experiments, we recorded the positron lifetime  $\tau$  at room temperature by using a conventional fast-fast coincidence spectrometer with a time resolution of  $R \approx 220$  ps. For that purpose, a <sup>22</sup>Na positron source was sandwiched between two identical samples. Approximately two million events were collected for each spectrum. After subtracting the source and background components, the lifetime spectra were fitted to the following expression:

$$L(t) = R \otimes \sum_i I_i \exp(-t/\tau_i). \quad (1)$$

Depending on the sample, the experimental data were fitted with one or two positron lifetime components ( $\tau_i$ ) using a modified version of the software POSFIT,<sup>21</sup> taking into account the convolution with the instrumental resolution  $R$ . For a two-component decomposition, we used  $L(t) = R \otimes [I_1 \exp(-t/\tau_1) + I_2 \exp(-t/\tau_2)]$ , where  $I_1$  and  $I_2$  are the intensities ( $I_1 + I_2 = 1$ ), and  $\tau_1$  and  $\tau_2$  are the two lifetime components of the spectra. The average lifetime was calculated as  $\tau_{av} = I_1 \tau_1 + I_2 \tau_2$ , and it increases when the size or/and the concentration of vacancy defects increases.

As a second technique, we carried out Doppler annihilation-ray broadening spectrometry by measuring the positron-electron momentum distributions at 300 K coupled to a slow monoenergetic positron beam. Because the momentum distribution of electrons in vacancy defects differs from that in bulk materials, these defects can be detected by measuring the Doppler broadening spectra of annihilation radiation, characterized by line-shape parameters  $S$  and  $W$ . The  $S$  parameter mainly reflects the change due to the annihilation of positron-electron pairs with a low-momentum distribution while  $W$  reflects the change due to the annihilation of positron-electron pairs with a high-momentum distribution. The reduced valence and core electron densities at vacancies increase the positron lifetime and narrow the positron-electron momentum distribution (so  $S$  increases and  $W$  decreases). The low- $S$  and high- $W$  momentum annihilation fractions in our experiments were measured in the momentum range  $(0 - 2.80) \times 10^{-3} m_0 c$  and  $(10.61 - 26.35) \times 10^{-3} m_0 c$ , respectively, whatever the value of the positron energy. The  $S$  and  $W$  values were recorded as a function of the positron energy  $E$  between 0.5 and 25.0 keV by 0.5 keV steps using a slow positron beam at the CEMHTI Site Cyclotron, CNRS Orléans.<sup>22</sup> The positron mean implantation depth in STO varied from  $\approx 2$  to  $\approx 1200$  nm in this energy range.<sup>23,24</sup> The positron implantation profiles are represented in Fig. 1 for several positron incident energies in the range  $E = 5 - 25$  keV. The knowledge of the  $S$  and  $W$  values provide us with relevant information. On one hand, once the positron implantation profile is known, from the dependence of  $S$  and  $W$  on the positron incident energy  $E$ , one can extract the vacancy-defect depth distribution profile using VEPFIT (Refs. 25 and 26) (see Sec.

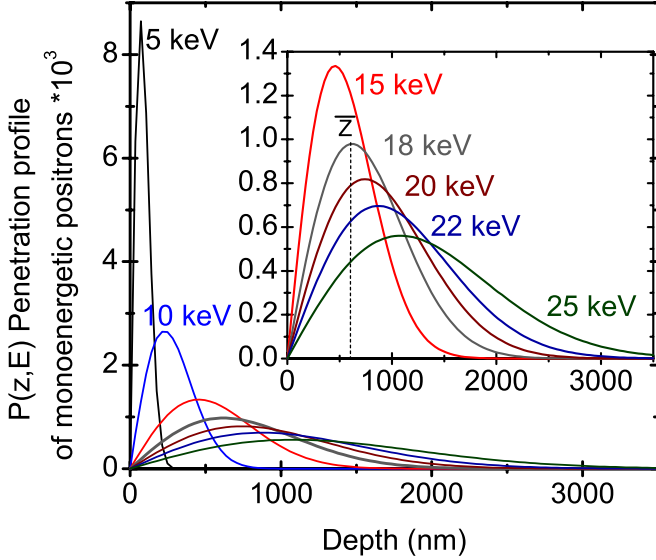


FIG. 1. (Color online) Positron depth profile in STO calculated for indicated positron incident energies according to Ref. 24 with the parameters  $A=2.95 \mu\text{g cm}^{-2} \text{keV}^{-r}$ ,  $m=2$ , and  $r=1.7$ . The inset shows a zoom of the data in the main panel, for positron incident energies between 15 and 25 keV. The dashed line in the inset indicates the mean penetration depth  $\bar{z}$  for 18 keV.

V for details). On the other hand, we can also obtain information about the concentration and nature of the vacancy defects from the knowledge of  $S$  and  $W$ . Indeed, if the  $(S, W)$  measured parameters are aligned on a straight line which goes through both the  $(S, W)$  data of the material lattice and the  $(S, W)$  characteristics of a defect  $V$ , it means that only one kind of defect  $V$  is present in the sample.<sup>27</sup>

### III. RESULTS (I): POSITRON LIFETIME SPECTRA AND IDENTIFICATION OF NATIVE VACANCY DEFECTS IN AS-RECEIVED SUBSTRATES

The positron lifetime spectra  $L(t)$  allowed to identify the IA-LAO sample as the defect-free STO lattice whereas as-received substrates were found to contain native vacancy defects. The optimal fittings to Eq. (1) were obtained when using one-lifetime component in IA-LAO and two for the as-received substrates. In Fig. 2, we show the measured spectra, together with the fittings and the instrumental resolution curve. In the following, we describe in more detail these experiments.

The spectra measured in the IA-LAO sample (Fig. 2) showed a room-temperature positron lifetime of  $\tau_{\text{IA-LAO}} \approx 154.4 \pm 0.3$  ps. This value is in good agreement with the experimental and calculated positron lifetime values in defect-free bulk STO ( $\tau_b \approx 138\text{--}156$  ps).<sup>7,17,28</sup> Because of the close agreement between the positron lifetimes of IA-LAO and defect-free bulk STO, we can assume from now on that the sample IA-LAO represents the STO lattice, free of vacancy defects. Now we turn to the positron lifetime spectra recorded in IE1000 and IE10 samples before any ion etching. The measured spectra were decomposed into two lifetime components  $\tau_1$  and  $\tau_2$  (Fig. 2). Assuming that the

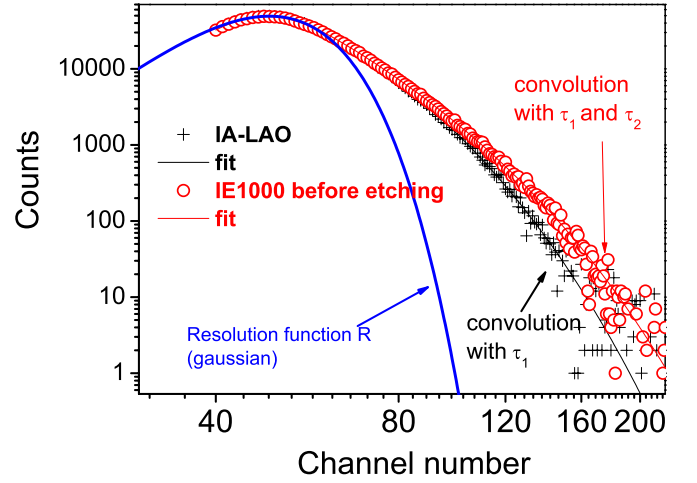


FIG. 2. (Color online) Positron lifetime spectra of samples IA-LAO and IE1000 before etching. The Gaussian instrumental resolution and the fittings to Eq. (1) are also shown.

positron is trapped by only one open-volume defect type (simplest trapping model, see Ref. 14), one can calculate  $1/\tau_{\text{mode}} = I_1/\tau_1 + I_2/\tau_2$ . We obtained a value  $\tau_{\text{mode}} \approx 152.5$  ps, i.e., close to the defect-free value observed in the IA-LAO sample. This agreement between  $\tau_{\text{mode}}$  and  $\tau_b$  means that the trapping of positrons occurs only in one type of vacancy defect.<sup>14</sup> The short component was found to be  $\tau_1 \approx 109.1 \pm 5.4$  ps with a relative intensity  $I_1 = 36\%$ . In the two-state trapping model, the lifetime  $\tau_1$ , often called the “reduced bulk lifetime”,<sup>14</sup> is shorter than the bulk lifetime due to a combination of positrons leaving the bulk state both by annihilation from it, and by trapping into a vacancy. In contrast, the long lifetime component had a value  $\tau_2 \approx 195.9 \pm 2.9$  ps with relative intensity  $I_2 = 64\%$ , indicating that the majority of the positrons in as-received substrates are trapped in this vacancy defect. According to the calculations, the lifetimes of positrons trapped by Ti vacancies ( $V_{\text{Ti}}$ ) is  $\tau_{\text{Ti}} \approx 170\text{--}200$  ps.<sup>17</sup> We assume therefore that Ti vacancies are present in as-received STO substrates before  $\text{Ar}^+$  etching. In view of these results, the nondetection of vacancy defects in the oxygen-annealed IA-LAO samples appears as an unexpected outcome. Further analysis is required to understand the nature of vacancy defects in as-received substrates and the precise effect of annealings on them.

### IV. RESULTS (II): DOPPLER ANNIHILATION-PAIR BROADENING SPECTROSCOPY

The low- $S$  and high- $W$  momentum annihilation fractions were measured over the first micron below the surface as a function of the incident positron energy  $E$ . Only the normalized  $S$  fraction is plotted for each sample in Fig. 3 (the  $W$ - $E$  curves mirror the  $S$ - $E$  data and are not represented here). We describe in the following the experimental  $S$ - $E$  curves for three different types of samples, i.e., as-received, ion-etched, and substrates reduced during thin-film growth.

In as-received substrates, the low fraction  $S$  values decrease down to 5 keV. This decrease has a strong contribu-



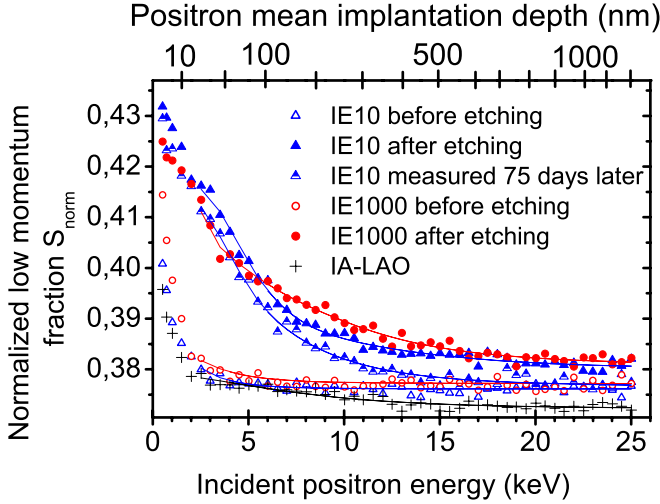


FIG. 3. (Color online) Normalized low-momentum annihilation fraction  $S$  vs incident positron energy  $E$  for sample IA-LAO and samples IE10 and IE1000 before and after  $\text{Ar}^+$  etching. Lines are the result of experimental data fitting using VEPFIT (Refs. 25 and 26). The fitting parameters are summarized in Table I. The derived depth distributions are shown in Fig. 5.

tion from surface effects (i.e., annihilation of positrons and positronium atoms on the sample surface), and does not reflect the intrinsic positron annihilation associated to vacancy defects. However, above 5 keV, the  $S$ - $E$  curves remain stable on a plateau, indicating a homogeneous depth distribution of vacancy defects. This constant value at high  $E$  indicates that in this energy range almost all positrons are implanted into the sample and annihilate in it without diffusing back to the surface region. The IA-LAO sample exhibits a similar trend but the plateau at energies above 5 keV has significantly lower  $S$  values than those corresponding to the as-received substrates, consistent with the virtually vacancy-free state of this sample.

On the contrary, for samples after  $\text{Ar}^+$  etching, the  $S$  parameter exhibits a different shape, meaning that a change in nature or concentration of defects occurs. For samples IE1000 and IE10 measured just after surface etching,  $S$  continuously decreases with the energy up to 15 keV, and then forms a plateau, indicating a nonhomogeneous depth distribution of vacancy defects. This  $S$  plateau is higher than before ion etching, meaning that the concentration of vacancy-type defects is higher after  $\text{Ar}^+$  etching, and it is extended even beyond 1  $\mu\text{m}$  from the surface (see VEPFIT simulation results below). We have recently discussed this strikingly large extension of the defect distribution in terms of a large diffusion of oxygen-vacancy complexes.<sup>29</sup> In addition, we have observed that the  $S$  parameter evolves with time. When the sample IE10 was measured 75 days later than the first measurement, we observed a clear reduction in  $S$  (Fig. 3), indicating a suppression of vacancy defects, probably related to the reoxygenation of the sample with time. This result is consistent with the observed suppression of the metallic behavior of the IE10 sample with time (see above): indeed, the sample became eventually insulating in the scale of a few days.

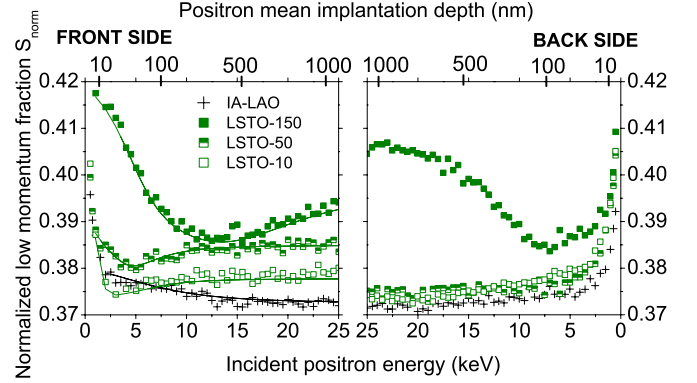


FIG. 4. (Color online) Normalized low-momentum annihilation fraction  $S$  vs incident positron energy  $E$  for the substrates depleted of oxygen during thin-film deposition (LSTO series, frontside, and backside experiments). The IA-LAO data are also shown as the reference of the defect-free STO lattice. Lines represent the fittings using VEPFIT (Refs. 25 and 26). The fitting parameters are summarized in Table I. The derived depth distributions are shown in Fig. 6.

Finally, we discuss the  $S$ - $E$  curves for samples reduced during the thin-film growth. In this case, the spectra were measured by implanting positrons both on the frontside and the backside (Fig. 4). The recorded experimental data indicate that the vacancy defects generated in the STO substrate during the low-pressure film deposition reached the backside of the substrates (this observation is more evident for the LSTO-150 sample but also the  $S$  values of LSTO-50 and LSTO-10 samples are higher than the  $S$  values of the reference IA-LAO, see Fig. 4). In addition, we observe that the  $S$  values increase with thickness, implying that the vacancy-defect content in the samples grows with the total deposition time. These results confirm the conclusions of our previous works concerning the fast diffusion of vacancies in the STO substrates during the film deposition<sup>8–10,30</sup> and are in agreement with previous reports on homoepitaxial growth on STO substrates by low-pressure molecular-beam epitaxy.<sup>7</sup> We observe also that both in the frontside and backside spectra, a small dip in the  $S$ - $E$  curves signals a slight depletion of vacancy defects on a subsurface region. This feature has been suggested to be due to some room-temperature reoxygenation induced by the atmospheric oxygen,<sup>7</sup> a phenomenon similar to that occurring in the IE10 sample measured 75 days later (see above). We comment more on this issue below when discussing the diffusion lengths of the implanted positrons.

## V. RESULTS (III): POSITRON DIFFUSION LENGTHS AND EXTRACTED DEPTH PROFILES OF VACANCY DEFECTS

The knowledge of the positron diffusion lengths and the vacancy-defect depth distributions was obtained by the simulation of the spectra representing the variation in the  $S$  and  $W$  parameters as a function of  $E$  discussed in the previous section. For that purpose, we used the VEPFIT code,<sup>25</sup> a computer program developed by van Veen *et al.*,<sup>26</sup> which takes into account the diffusion of the implanted positrons into the ma-

TABLE I. Summary of VEPFIT fitting results for samples indicated in the first column. We show the fitted  $S$  and  $W$  values for each layer used in the model, along with the effective diffusion length ( $L_+^i$ ) and depth of the layer boundaries ( $B_i$ ); errors are given within brackets, and those quantities fixed in the fit are marked with (F). The reduced  $\chi^2$  values are also given.

Sample	Layer 1				Layer 2				Layer 3				$\chi^2$ ( $S$ )	$\chi^2$ ( $W$ )
	$S_1$	$W_1$	$L_+^1$ (nm)	$B_1$ (nm)	$S_2$	$W_2$	$L_+^2$ (nm)	$B_2$ (nm)	$S_3$	$W_3$	$L_+^3$ (nm)			
IA-LAO	0.3725 (1)	0.0750 (1)	200.2 (15.3)										0.84	0.90
IE10 before etching	0.3765 (1)	0.0725 (0)	21.3 (1.6)										1.12	1.17
IE10 after etching	0.4117 (7)	0.0590 (3)	12.0 (F)	92 (3)	0.3834 (3)	0.0709 (1)	20.0 (F)	658 (39)	0.3803 (3)	0.0730 (2)	21.3 (F)		1.54	1.34
IE10 75 days later	0.4062 (8)	0.0608 (4)	12.0 (F)	84 (2)	0.3813 (5)	0.0709 (2)	20.0 (F)	333 (17)	0.3766 (2)	0.0734 (1)	21.3 (F)		1.88	1.91
IE1000 before etching	0.3771 (1)	0.0723 (0)	34.9 (1.6)										1.16	1.33
IE1000 after etching	0.3989 (4)	0.0644 (2)	12.0 (F)	148 (6)	0.3888 (5)	0.0680 (2)	20.0 (F)	417 (13)	0.3810 (2)	0.0726 (1)	34.9 (F)		1.82	1.63
LSTO-10	0.2535 (158)	0.1281 (86)	12.0 (0)	11 (F)	0.3756 (5)	0.0763 (3)	30.0 (F)	199 (16)	0.3778 (2)	0.0739 (1)	25 (F)		1.25	1.72
LSTO-50	0.3825 (9)	0.0752 (5)	10.0 (2)	50 (F)	0.3759 (11)	0.0756 (6)	30.0 (F)	143 (6)	0.3849 (2)	0.0723 (1)	25 (F)		1.45	1.95
LSTO-150	0.3989 (58)	0.0576 (29)	159.0 (20)	150 (F)	0.3836 (3)	0.0716 (1)	30.0 (F)	1049 (21)	0.3978 (6)	0.0689 (3)	25 (F)		1.46	1.41

terial. The analysis of these data for different energies, and hence depths, is achieved by splitting the material into a series of layers. For each layer, the VEPFIT program determines the fraction of positrons that annihilates at a given depth of a material, and the corresponding  $S$  and  $W$  parameters are calculated as follows:

$$S(E) = S_S \times f_S(E) + \sum_i S_i \times f_i(E), \quad (2)$$

where  $f_S(E)$  is the fraction of positrons annihilated at the surface, and  $f_i(E)$  is the fraction annihilated in the layer  $i$ . The  $S_S$  and  $S_i$  parameters are the low-momentum annihilation fractions  $S$  at the surface and layer  $i$ , respectively. The same equation is used for  $W$ . For each individual layer  $i$ , a given positron effective diffusion length  $L_+^i$  was also assumed. The conventional Makhovian positron implantation profile was used (Fig. 1), and both one-, two- and three-layer models for the different samples were considered, along with a density of  $5.175 \text{ g cm}^{-3}$  calculated for STO. The variables that could be fitted or fixed were the  $S_i$  and  $W_i$  in each layer  $i$ , as well as the thickness  $B_i$  of each layer, and the effective positron diffusion length  $L_+^i$ , which are reported in Table I. We excluded from the analysis the data corresponding to incident positron energies below 2 keV, to rule out any spurious surface effects. We found that the best fittings for as-received nonetched STO substrates and postannealed LAO/STO samples were obtained assuming one single layer in the model whereas for the ion-etched substrates, a three-layer model should be assumed (see Table I). The VEPFIT fitting results summarized in Table I are plotted in Figs. 5 and 6 for a better visualization.

First we discuss the effective positron diffusion lengths obtained from the VEPFIT fittings and displayed in Table I. For the IA-LAO sample, the effective diffusion length was  $L_+ \approx 200 \pm 15 \text{ nm}$ , i.e., close to typical values of  $L_+$  in semiconductor materials (200–300 nm) such as Si,<sup>31</sup> and those in metals (150–200 nm) such as Ni.<sup>32</sup> Such high value of positron diffusion length means that few or no vacancy defects are detected in the sample IA-LAO—in agreement with the experimental positron lifetime experiments described above.

On the contrary, much shorter effective diffusion lengths—between 10 and 35 nm—were found in as-received STO substrates. These values are consistent with previous studies where values in the range 2–50 nm have been reported in perovskite oxide materials containing oxygen-related and other defects.<sup>7,16</sup> We attribute such short positron diffusion lengths to the presence of Ti vacancies (see above the description of positron lifetime spectra) in the as-received substrates.

In contrast to the previous samples, the spectra of the ion-etched samples (IE1000 and IE10) and the samples reduced during thin-film deposition (LSTO-10, LSTO-50, and LSTO-150) were fitted using a three-layered model. This choice was driven mainly by the quality of the fittings of the VEPFIT simulations, i.e., by the values of the resulting reduced chi-squared values ( $\chi^2 < 2$  was used as a quality standard).<sup>33</sup> We illustrate the procedure used for these samples with the particular case of the sample IE10 after etching. For this sample, we observed that the best fittings were obtained by fixing the  $L_+$  value and using three layers

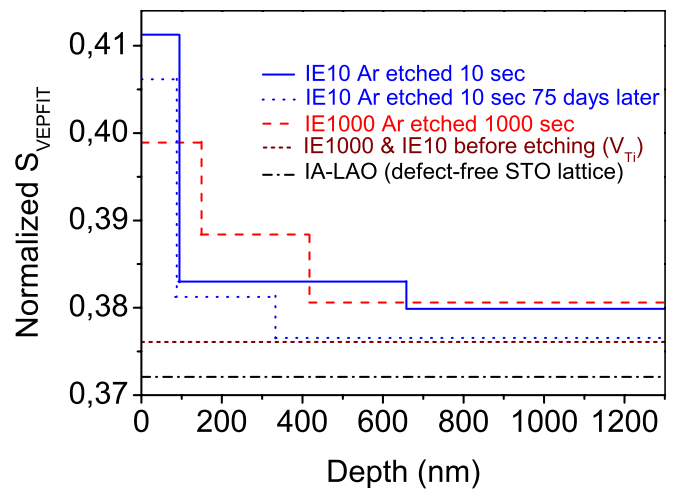


FIG. 5. (Color online) Depth profile of vacancy defects in ion-etched and as-received substrates probed by positrons in STO, extracted from VEPFIT spectra simulation.

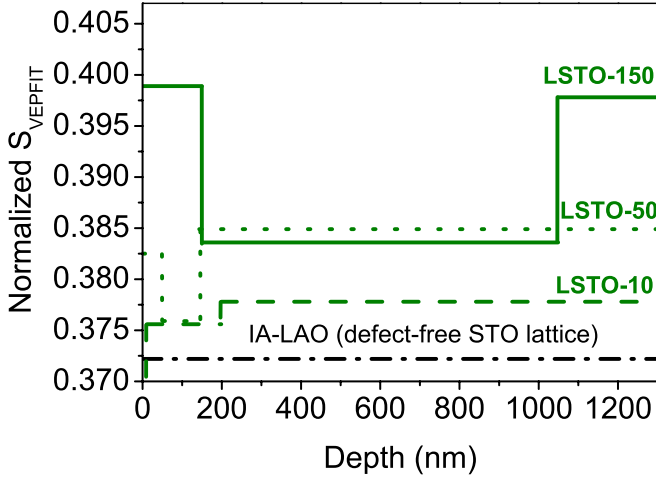


FIG. 6. (Color online) Depth profile of vacancy defects in substrates reduced during film deposition probed by positrons in STO, extracted from VEPFIT spectra simulation.

(see Fig. 7 and Table II). Note that, in spite of the low chi-squared values, we discarded the fitting with just one layer and free  $L_+$  because of the unphysical large  $L_+$  value resulting from those fittings. Using similar fitting protocols we found that for the ion-etched samples, the optimal fittings were obtained if we fixed the positron effective diffusion length in the deeper layer (layer 3) to the value obtained in the samples before etching, i.e.,  $L_+^3=21.3$  and  $L_+^3=34.9$  nm for samples IE1000 and IE10 (Table I), respectively. After several fitting tests, the best reproducible spectra were obtained when the diffusion length in layer 1 (close to the surface) was fixed to  $L_+^1=12$  nm and in the second layer to  $L_+^2=20$  nm. These values are similar to those measured in as-received substrates, indicating the expected presence of vacancy defects after ion etching. For the samples reduced during film deposition, the positron effective diffusion lengths were fixed except in layer 1, and the layer boundaries  $B_i$  were fixed to 11 nm, 50 nm, and 150 nm, respectively.

Let us turn now to the normalized  $S(S_{\text{VEPFIT}})$  values obtained from the VEPFIT fittings, which are known to be proportional to the vacancy-defect concentration. We first discuss the as-received and the ion-etched data (Fig. 5) and, subsequently, we analyze the growth-assisted samples (Fig. 6). We have shown above that vacancy defects in samples

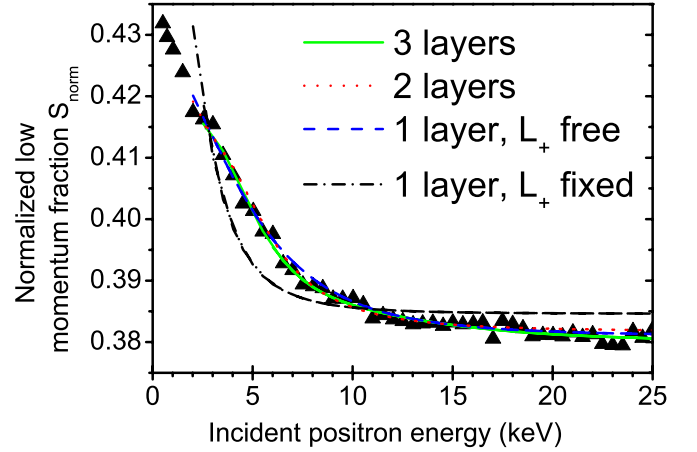


FIG. 7. (Color online) Normalized low-momentum annihilation fraction  $S$  vs incident positron energy  $E$  for sample IE10 after etching. Lines are the result of experimental data fitting to the VEPFIT software using one layer and free  $L_+$  (dashed), and fixed  $L_+$  with one (dashed dotted), two (dotted), and three (solid) layers. The resulting fitting parameters are summarized in Table II.

IA-LAO and as-received IE1000 and IE10 are homogeneously distributed in depth (cf. Fig. 3). Thus, it is not unreasonable that the best VEPFIT fittings were obtained assuming one single layer for these samples, i.e.,  $S_{\text{VEPFIT}}$  takes the same value for all depth values (Fig. 5). The lowest  $S_{\text{VEPFIT}}$  values are those obtained for sample IA-LAO, which according to our previous discussion can be assumed to be equivalent to the defect-free STO lattice (Fig. 5). In contrast,  $S_{\text{VEPFIT}}$  is higher for as-received substrates (IE1000 and IE10 before etching in Fig. 5) due to the presence of Ti vacancies. In contrast, a nonhomogeneous depth profile of vacancy defects is observed after  $\text{Ar}^+$  etching (Fig. 5), with vacancy defects extending deep beyond  $1 \mu\text{m}$  from the irradiated surface. We further note that the  $S_{\text{VEPFIT}}$  of sample IE10 measured 75 days after ion etching exhibits the same values as those of nonetched samples for depths larger than  $\approx 350$  nm, consistent with a relatively fast reoxygenation with time of sample IE10.

The vacancy depth profile of growth-assisted reduced samples is shown in Fig. 6. From these data, we emphasize two relevant aspects. First, we observe that, consistent with the raw as-measured  $S$ - $E$  data, the depth profiles in this figure also show a region depleted in vacancy defects

TABLE II. Comparison of VEPFIT results concerning the IE10 sample for different number of layers indicated in the first column. The fitted  $S$  and  $W$  values for each layer used in each model, along with the effective diffusion length ( $L_+^i$ ) and depth of the layer boundaries ( $B_i$ ), are shown: errors are given within brackets, and quantities fixed in the fittings are marked with (F). The reduced  $\chi^2$  values are also given.

Sample IE10	Layer 1				Layer 2				Layer 3			$\chi^2$ ( $S$ )	$\chi^2$ ( $W$ )
	$S_1$	$W_1$	$L_+^1$ (nm)	$B_1$ (nm)	$S_2$	$W_2$	$L_+^2$ (nm)	$B_2$ (nm)	$S_3$	$W_3$	$L_+^3$ (nm)		
1 layer, free $L_+$	0.3809 (2)	0.0723 (1)	90.3									1.64	1.33
1 layer, fixed $L_+$	0.3846 (1)	0.0706 (1)	21.3 (F)									33.22	27.46
2 layers, fixed $L_+$	0.0493 (5)	0.0597 (3)	12.0 (F)	107 (1)	0.3817 (2)	0.0719 (1)	21.3 (F)					2.10	2.18
3 layers, fixed $L_+$	0.4117 (7)	0.0590 (3)	12.0 (F)	92 (3)	0.3834 (3)	0.0709 (1)	20 (F)	658 (39)	0.3803 (3)	0.0730 (2)	21.3 (F)	1.54	1.34

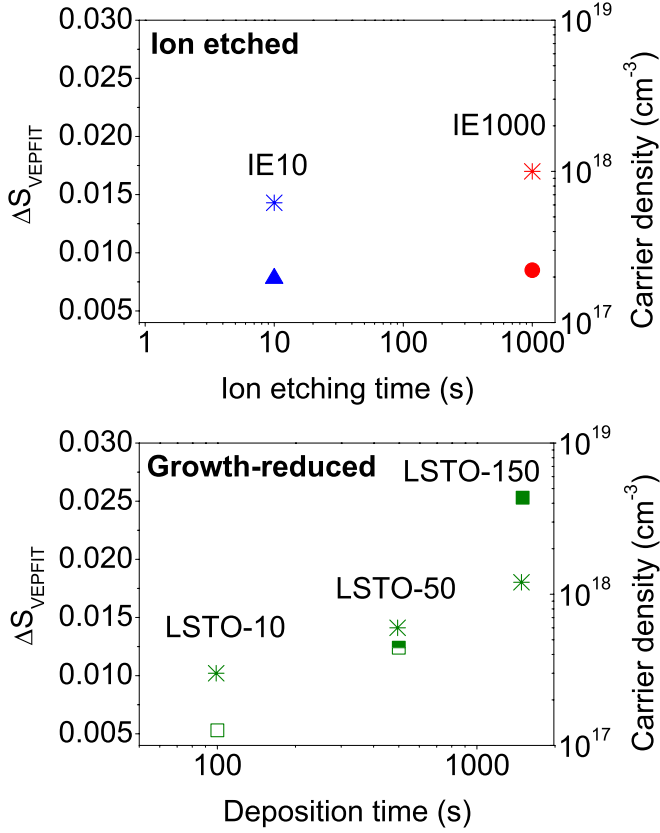


FIG. 8. (Color online) Plot of  $\Delta S_{\text{VEPFIT}}$  and vacancy concentration as a function of ion-etching time (upper panel, samples IE10 and IE1000) and of film deposition time (lower panel, substrates depleted of oxygen during film deposition, LSTO series). The carrier density data are indicated by asterisk symbols in both panels.

below the surface. Second, we observe that the deeper layers below this subsurface region have a vacancy content that increases with thickness, i.e., with film deposition time. This important observation is linked to our recent report on carrier density doping of STO substrates controlled by thin-film deposition.<sup>10</sup> It is our intention here to deal with this issue from the point of view of the PAS analysis. For that purpose, we have taken the IA-LAO  $S_{\text{VEPFIT}}$  value as the vacancy-free reference, and plotted  $\Delta S_{\text{VEPFIT}} = [S_{\text{VEPFIT}}(\text{LSTO}) - S_{\text{VEPFIT}}(\text{IA-LAO})]$  as a function of the film deposition time (see lower panel of Fig. 8), where the  $S_{\text{VEPFIT}}(\text{LSTO})$  values refer to the deeper layer (layer 3) in samples reduced during the film growth. We see in this figure that both  $\Delta S_{\text{VEPFIT}}$  and the carrier density  $n$  increase with the deposition time thus supporting our previously outlined scenario, i.e., that vacancy and carrier concentrations are both controlled via thin-film deposition parameters.<sup>10</sup> We have completed this study by plotting in the upper panel of Fig. 8 the values of  $\Delta S_{\text{VEPFIT}}$  and the carrier concentration  $n$  of the ion-etched samples, showing that both  $\Delta S_{\text{VEPFIT}}$  and  $n$  increase with the irradiation time. Note that the  $\Delta S_{\text{VEPFIT}}/n$  ratio varies between ion-etched and growth-reduced samples. This fact may result from the uncertainty in the determination of  $n$  from Hall experiments, especially in ion-etched samples where the carrier spatial distribution is inhomogeneous.<sup>10</sup>

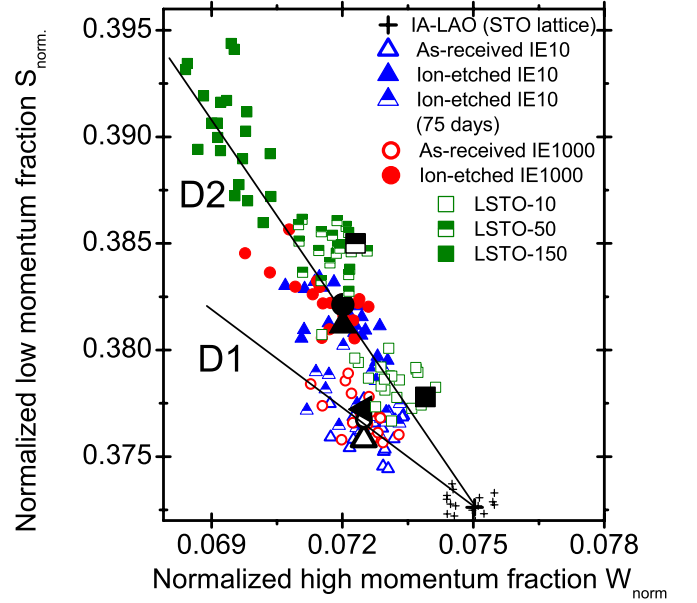


FIG. 9. (Color online) Normalized low annihilation fraction  $S$  vs normalized high annihilation fraction  $W$  for sample IA-LAO and samples IE1000 and IE10 before and after  $\text{Ar}^+$  etching during, respectively, 1000 s and 10 s. Data of the LSTO series (substrates depleted of oxygen during film deposition) are also plotted. Only  $(S, W)$  points measured between 15 and 25 keV, i.e., where a plateau is observed (see Figs. 3 and 4), are represented on this graph.  $(S, W)$  values averaged between 15 and 25 keV are represented in black (same symbols as raw data, bigger size).

## VI. RESULTS (IV): NATURE OF THE VACANCY DEFECTS AFTER ION ETCHING

The determination of the nature of the vacancy defects induced by  $\text{Ar}^+$  etching as well as low-oxygen pressure film growth can be obtained by plotting the normalized low-momentum annihilation fraction  $S$  versus the normalized high-momentum annihilation fraction  $W$ .<sup>14</sup> Only the  $(S, W)$  points measured between 15 and 25 keV are represented in Fig. 9, where a plateau is observed in the  $S$  vs  $E$  graph (Figs. 3 and 4). From these results we conclude that: (i) a straight line (D1) is obtained between the characteristic  $(S, W)$  points of the STO lattice (IA-LAO) and samples IE1000 and IE10 before etching, as well as in sample IE10 after  $\text{Ar}^+$  etching measured 75 days later. This means that the same main type of vacancy defects is detected by the positrons in as-received STO substrates and in sample IE10 after  $\text{Ar}^+$  etching measured 75 days later, most probably  $\text{Ti}$  vacancy defects ( $V_{\text{Ti}}$ ), as mentioned above.

(ii) Another straight line (D2) is observed between the characteristic  $(S, W)$  points of the STO lattice (IA-LAO) and those of samples IE1000 and IE10 measured just after the  $\text{Ar}^+$  etching and all films of the LSTO series. This mere observation implies that the same vacancy defects are generated either by etching the surface ions or by reduction in the crystals during low-pressure growth. In addition, we observe that the slope of D2 is larger than that of D1, meaning that a neutral or negatively-charged vacancy defect with a larger size than  $V_{\text{Ti}}$  is detected by positrons.<sup>34</sup> Thus, divacancies or



larger vacancies are created in STO after  $\text{Ar}^+$  etching. Since oxygen-related vacancies are likely to be introduced during the  $\text{Ar}^+$  etching<sup>12,35</sup> and low-oxygen pressure growth,<sup>9,10,30</sup> one can speculate that the observed D2 line might be attributed to  $V_{\text{Ti}}V_{\text{O}}$ ,  $V_{\text{Sr}}V_{\text{O}}$ , or  $V_{\text{O}}V_{\text{O}}$  divacancies, in detriment of divacancies such as  $V_{\text{Sr}}V_{\text{Ti}}$  or  $V_{\text{Ti}}V_{\text{Ti}}$ . Conversely, a recent work has demonstrated that for vacuum-annealed and electron-irradiated STO crystals, the positron lifetime spectra could be explained by the formation of Sr vacancies and their complexes with nearest-neighbor oxygen vacancies<sup>17</sup> so these defects could also be associated with the D2 slope in the (*S*-*W*) plot of ion-irradiated STO crystals. This picture seems also to be supported by first-principles calculations showing that defect complexes involving Sr vacancies have low formation energies.<sup>36,37</sup> Further work is needed to determine precisely the nature of vacancy defects created by  $\text{Ar}^+$  etching and low-pressure growth. As an example, temperature-dependent measurements should help determining the nature of vacancy defects after ion etching.

## VII. CONCLUSIONS

We have carried out an extensive study of the nature and spatial distributions of vacancy defects in STO substrates treated under different conditions: as-received, oxygen-annealed, and oxygen-depleted substrates have been analyzed by means of positron-annihilation spectroscopies. The STO substrates with oxygen content depleted either by ion etching or thin-film growth exhibit high-mobility conduction (typically well above  $10^3 \text{ cm}^2/\text{Vs}$ ). From our analysis, we have demonstrated that the as-received substrates contain a uniform distribution of native Ti vacancies, which are the main point defect in these samples. Upon oxygen treatment at high temperature, these defects appear to be annealed and the resulting substrates appear to be virtually free of vacancy defects. This unexpected outcome deserves a further detailed study to investigate whether native Ti vacancy defects in as-received substrates are associated to interstitial-vacancy pair defects which can be annealed at high temperature. We also note that although in our annealed LAO/STO samples, the STO substrates exhibit a vacancy concentration even lower than that of as-received substrates, the present experiments cannot provide the required resolution to probe the presence of vacancy defects at the LAO/STO interface because of the ultrathin thickness (few unit cells) of LAO lay-

ers and the fact that positron-electron pair annihilations induced by the surface may mask the intrinsic effect in the solid. In addition, we emphasize that positron-annihilation spectroscopies are essentially sensitive to vacancy defects and not to substitutional-type defects.

Conversely, in conductive oxygen-depleted substrates, the main vacancy-defect type is the same for both room-temperature ion-etched and high-temperature growth-assisted reduced samples, i.e., cation-oxygen vacancy complexes such as titanium-oxygen ( $V_{\text{Ti}}V_{\text{O}}$ ), oxygen-oxygen ( $V_{\text{O}}V_{\text{O}}$ ), or strontium-oxygen ( $V_{\text{Sr}}V_{\text{O}}$ ) divacancies. The spatial distribution of these vacancy-defect complexes is strongly dependent on the treatment conditions. In substrates doped during low-oxygen pressure and high-temperature film deposition, these vacancies are spread throughout the whole substrate and reach its backside. In contrast, in room-temperature ion-etched substrates, the vacancy defects are spread nonuniformly within a region extended a few microns below the surface. These results highlight the fast diffusion of oxygen-vacancy complexes in STO substrates. We have also shown that atmospheric oxygen can be incorporated at room-temperature conditions in these oxygen-depleted substrates. Our positron-annihilation spectroscopy experiments demonstrates that there is a subsurface region within the micron scale where the cation-oxygen vacancy complexes can be annealed at room temperature over scale of times as short as a few weeks. Our results are relevant to understand the transport mechanism on  $\text{SrTiO}_3$ -based three- and two-dimensional electron gases based on the vacancy-doping mechanism and can give insights into defect engineering to build oxide nanostructures such as quantum wells, wires, or dots.

## ACKNOWLEDGMENTS

This work is supported by French Research Agency program “OXITRONICS” under Contract No. ANR-08-BLAN-0237-01 and the PICS-CNRS “POSTIT” Project. Financial support from Croatian MZOS Project No. 119-1191458-1023 and France-Croatia COGITO program No. 19636YM (HOMMES) are also acknowledged. A.G. acknowledges discussions on positron-annihilation data analysis with Aurélien Debelle (CSNSM-Orsay) and Marie-France Barthe (CEMHTI-Orléans), and technical assistance of Virginie Moineau and Pierre Desgardin (CEMHTI-Orléans) during PAS experiments.

\*gherranz@icmab.es

<sup>1</sup>J. H. Haeni, P. Irvin, W. Chang, R. Uecker, P. Reiche, Y. L. Li, S. Choudhury, W. Tian, M. E. Hawley, B. Craigo, A. K. Tagantsev, X. Q. Pan, S. K. Streiffer, L. Q. Chen, S. W. Kirchoefer, J. Levy, and D. G. Schlom, *Nature (London)* **430**, 758 (2004).

<sup>2</sup>H. P. R. Frederikse and W. R. Hosler, *Phys. Rev.* **161**, 822 (1967).

<sup>3</sup>K. Bouzehouane, P. Woodall, B. Marcilhac, A. N. Khodan, D. Crété, E. Jacquet, J. C. Mage, and J. P. Contour, *Appl. Phys. Lett.* **80**, 109 (2002).

*Lett.* **80**, 109 (2002).

<sup>4</sup>K. Szot, W. Speier, G. Bihlmayer, and R. Waser, *Nature Mater.* **5**, 312 (2006).

<sup>5</sup>M. Janousch, G. I. Meijer, U. Staub, B. Delley, S. F. Karg, and B. P. Andreasson, *Adv. Mater.* **19**, 2232 (2007).

<sup>6</sup>O. N. Tufte and P. W. Chapman, *Phys. Rev.* **155**, 796 (1967).

<sup>7</sup>A. Uedono, K. Shimayama, M. Kiyohara, and Z. Q. C. K. Yamabe, *J. Appl. Phys.* **92**, 2697 (2002).

<sup>8</sup>M. L. Scullin, C. Yu, M. Huijben, S. Mukerjee, J. Seidel, Q.

- Zhan, J. Moore, A. Majumdar, and R. Ramesh, *Appl. Phys. Lett.* **92**, 202113 (2008).
- <sup>9</sup>G. Herranz, M. Basletic, M. Bibes, R. Ranchal, A. Hamzic, E. Tafr, K. Bouzehouane, E. Jacquet, J. P. Contour, A. Barthélmy, and A. Fert, *Phys. Rev. B* **73**, 064403 (2006).
- <sup>10</sup>G. Herranz, M. Basletic, O. Copie, M. Bibes, A. N. Khodan, C. Carrétéro, E. Tafr, E. Jacquet, K. Bouzehouane, A. Hamzic, and A. Barthélmy, *Appl. Phys. Lett.* **94**, 012113 (2009).
- <sup>11</sup>D. Reagor and V. Y. Butko, *Nature Mater.* **4**, 593 (2005).
- <sup>12</sup>D. Kan, T. Terashima, R. Kanda, A. Masuno, K. Tanaka, S. Chu, H. Kan, A. Ishizumi, Y. Kanemitsu, Y. Shimakawa, and M. Takano, *Nature Mater.* **4**, 816 (2005).
- <sup>13</sup>R. Krause-Rehberg, H. S. Leipner, T. Abgarjan, and A. Polity, *Appl. Phys. A: Mater. Sci. Process.* **66**, 599 (1998).
- <sup>14</sup>R. Krause-Rehberg and H. Leipner, *Positron Annihilation in Semiconductors, Solid-State Sciences* (Springer, Berlin, 1999), Vol. 127.
- <sup>15</sup>A. Uedono, M. Kiyohara, N. Yasui, and K. Yamabe, *J. Appl. Phys.* **97**, 033508 (2005).
- <sup>16</sup>S. McGuire, D. Keeble, R. Mason, P. Coleman, Y. Koutsonas, and T. Jackson, *J. Appl. Phys.* **100**, 044109 (2006).
- <sup>17</sup>R. A. Mackie, S. Singh, J. Laverock, S. B. Dugdale, and D. J. Keeble, *Phys. Rev. B* **79**, 014102 (2009).
- <sup>18</sup>M. Basletic, J.-L. Maurice, C. Carrétéro, G. Herranz, O. Copie, M. Bibes, É. Jacquet, K. Bouzehouane, S. Fusil, and A. Barthélmy, *Nature Mater.* **7**, 621 (2008).
- <sup>19</sup>A. D. Caviglia, S. Gariglio, N. Reyren, D. Jaccard, T. Schneider, M. Gabay, S. Thiel, G. Hammerl, J. Mannhart, and J.-M. Triscone, *Nature (London)* **456**, 624 (2008).
- <sup>20</sup>N. Reyren, S. Gariglio, A. D. Caviglia, D. Jaccard, T. Schneider, and J.-M. Triscone, *Appl. Phys. Lett.* **94**, 112506 (2009).
- <sup>21</sup>P. Kirkegaard and M. Eldrup, *Comput. Phys. Commun.* **3**, 240 (1972).
- <sup>22</sup>P. Desgardin *et al.*, *Mater. Sci. Forum* **363-365**, 523 (2001).
- <sup>23</sup>S. Valkealahti and R. Nieminen, *Appl. Phys. A* **35**, 51 (1984).
- <sup>24</sup>A. Vehanen, K. Saarinen, P. Hautojärvi, and H. Huomo, *Phys. Rev. B* **35**, 4606 (1987).
- <sup>25</sup>H. Schut and A. van Veen, *Appl. Surf. Sci.* **85**, 225 (1995).
- <sup>26</sup>A. van Veen, H. Schut, J. de Vries, R. A. Hakvoort, and M. R. Ijpma, in *Positron Beams for Solids and Surfaces*, edited by P. J. Schultz, G. R. Massoumi, and P. J. Simpson, AIP Conf. Proc. No. 218 (AIP, New York, 1990), p. 171.
- <sup>27</sup>K. Saarinen, P. Hautojärvi, J. Keinonen, E. Rauhala, J. Räisänen, and C. Corbel, *Phys. Rev. B* **43**, 4249 (1991).
- <sup>28</sup>D. J. Keeble, S. McGuire, S. Singh, B. Su, T. W. Button, and J. Petzelt, *J. Phys. IV* **128**, 111 (2005).
- <sup>29</sup>G. Herranz, O. Copie, A. Gentils, E. Tafr, M. Basletic, F. Fortuna, K. Bouzehouane, S. Fusil, É. Jacquet, C. Carrétéro, M. Bibes, A. Hamzic, and A. Barthélmy, *J. Appl. Phys.* (to be published).
- <sup>30</sup>G. Herranz, M. Basletic, M. Bibes, C. Carrétéro, E. Tafr, E. Jacquet, K. Bouzehouane, C. Deranlot, A. Hamzic, J.-M. Broto, A. Barthélmy, and A. Fert, *Phys. Rev. Lett.* **98**, 216803 (2007).
- <sup>31</sup>B. Nielsen, K. G. Lynn, D. O. Welch, T. C. Leung, and G. W. Rubloff, *Phys. Rev. B* **40**, 1434 (1989).
- <sup>32</sup>K. G. Lynn, D. M. Chen, B. Nielsen, R. Pareja, and S. Myers, *Phys. Rev. B* **34**, 1449 (1986).
- <sup>33</sup>The indicated reduced chi-squared values were obtained by dividing the values given by the VEPFIT program, by the number of degrees of freedom which is in our case the number of data points minus the number of fitted parameters.
- <sup>34</sup>M. Hakala, M. J. Puska, and R. M. Nieminen, *Phys. Rev. B* **57**, 7621 (1998).
- <sup>35</sup>D. Kan, O. Sakata, S. Kimura, M. Takano, and Y. Shimakawa, *Jpn. J. Appl. Phys., Part 2* **46**, L471 (2007).
- <sup>36</sup>M. J. Akhtar, Z. U. N. Akhtar, R. A. Jackson, and C. R. A. Catlow, *J. Am. Ceram. Soc.* **78**, 421 (1995).
- <sup>37</sup>T. Mizoguchi, Y. Sato, J. P. Buban, K. Matsunaga, T. Yamamoto, and Y. Ikuhara, *Appl. Phys. Lett.* **87**, 241920 (2005).